Proceedings of the ASME 37th International Conference on Ocean, Offshore and Arctic Engineering
OMAE2018
June 17-22, 2018, Madrid, Spain

OMAE2018-77308

PREVENTING THE ADDED-MASS INSTABILITY IN FLUID-SOLID INTERACTION FOR OFFSHORE APPLICATIONS

Arthur E.P. Veldman*
Henk Seubers
Peter van der Plas
Institute for Mathematics and Computer Science
University of Groningen
P.O. Box 407, 9700 AK Groningen
The Netherlands
{a.e.p.veldman, h.seubers, p.van.der.plas}@rug.nl

Matin Hosseini Zahraei
Peter R. Wellens
Rene H.M. Huijsmans
Department of Ship Hydrodynamcs
Delft University of Technology
Mekelweg 2, 2628 CD Delft
The Netherlands
{s.hosseinizahraei, p.r.wellens}@tudelft.nl

ABSTRACT

Simulating the hydrodynamics of deformable, floating structures using a partitioned strategy poses a major challenge when the ratio of the added mass to the structural mass is considerate. Existing computational procedures for fluid-structure interaction become less efficient or even unstable. In these situations, it is advisable to modify the coupling to allow the fluid to respond better to the solid motions. A simultaneous solution of the equations governing fluid and solid-body would be a stable choice but is often not feasible. Usually the numerical problems are taken care of with subiterations between fluid and structure, but their convergence can be slow. In this paper we present a more powerful, quasi-simultaneous approach, which tries to mimic a fully simultaneous coupling in an affordable way. It makes use of a simple approximation of the body dynamics, based on the (6 DOF) solid-body modes and the main elastic modes of the structure. The method will be demonstrated in offshore practice, with a falling life boat, a floating CALM buoy, an elastic membrane and a rubber gate.

1 INTRODUCTION

Traditionally, multi-physics problems are classified as 'strongly' or 'weakly' interacting. From a physical perspective, the interaction is called *weak* if one subsystem dominates the behavior of the coupled problem, and it is called *strong* if the subsystems 'have an equal say' in the interaction [1]. So the physical interaction strength is a scale running from a *one-way* hierarchy to a *two-way* interaction. An example of a hierarchy is the case of a very light particle in a large water wave: its motion follows completely from the motion of the unaffected wave. The exact opposite hierarchy occurs for heavy objects, like a tanker, in quiet water, where the flow of the water is completely determined by the ship's motion.

In hydrodynamic applications with moving or deforming structures, a major factor affecting the interaction strength is the ratio of the *added mass* of the fluid to the *structural mass* [2, 3]. In the traditional partitioned formulation, where the fluid loads are imposed on the structure and the structural motions imposed on the fluid, higher added mass ratios increase the interaction strength. In case of a physical two-way coupling, this leads to large amplification factors in the fluid-structure iterations, which cannot be controlled by reducing the time step (e.g. [4]). Usually, this effect is tackled by applying subiterations with severe underrelaxation within each time step, making these coupling methods computationally expensive (e.g. [5]).

The mentioned problems could be bypassed by solving the two subdomains in a monolithic way. Usually, this is complicated since the simulation methods for the subdomains have to be integrated down to the inner algorithmic loops. This requires

*Address all correspondence to this author.

access to both subdomain codes, which can be quite cumbersome and even impossible in case of black-box codes. Here we will follow an approach as close as possible to the monolithic, simultaneous approach. This *quasi-simultaneous* approach was originally developed to add viscous effects to inviscid airfoil simulations. There, a model of the viscous boundary layer along the airfoil surface is coupled to an inviscid flow model. In a point of flow separation, the strong interaction between the two subdomains of the flow introduces a singularity [1, 6] The quasi-simultaneous interaction method, presented to a wider CFD audience in [7, Ch. 16], overcomes these problems by solving a simplified (reduced order) model of the inviscid flow simultaneously with the boundary-layer equations. This model has been termed *interaction law* as it describes how the inviscid flow reacts to changes in the boundary layer. Algorithmically, this interaction law can be regarded (and implemented) as a boundary condition to the viscous-flow equations.

In the hydrodynamic applications we are discussing in this paper, the interaction law will be an approximate model for the structural equations, to be solved simultaneously with the flow equations. This simplified model will be built from the solid-body modes and the main elastic modes of the structure. The fluid solver in this study is the symmetry preserving finite-volume VOF method ComFLOW [8–12]. A finite element method is used to solve the elastic structure response based on a Euler-Bernoulli beam. Kinematic and dynamic relations couple fluid dynamics to the structural dynamics. Section 2 describes this mathematical model in more detail, together with the discretization strategy. Also, the weakness of the traditional coupling approaches is explained.

In Section 3, the stability of the numerical coupling between fluid and structure is analysed. The ratio of added fluid mass to structural mass appears to play an essential role. It requires the use of severe underrelaxation of the traditional coupling method. A more efficient approach is the quasi-simultaneous method, built around an 'interaction law' that globally describes the structural dynamics. By incorporating the interaction law into the system, the advantages of the quasi-simultaneous method are explained. In Section 4, the numerical stability with and without the interaction law is verified with a schematic test case. Finally, validation follows from an oscillating CALM buoy, a falling life boat, a tank with a flexible bottom and a dambreak behind a rubber gate, for each of which experimental data is available.

2 MATHEMATICAL MODEL

2.1 Flow model

Incompressible, turbulent fluid flow can be modelled by means of the Navier–Stokes equations.

$$M\mathbf{u} = 0, \qquad \frac{\partial \mathbf{u}}{\partial t} + C(\mathbf{u})\mathbf{u} + Gp - V\mathbf{u} = \mathbf{f}. \tag{1}$$

Here M is the divergence operator, which describes conservation of mass. Conservation of momentum is based on the convection operator $C(\mathbf{u})\mathbf{v} \equiv \nabla(\mathbf{u}\otimes\mathbf{v})$, the pressure gradient operator $G = \nabla$, the viscous diffusion operator $V(\mathbf{u}) \equiv \nabla\cdot\nu\nabla\mathbf{u}$ and a forcing term $\mathbf{f}$. The kinematic viscosity is denoted by ν. Turbulence is modelled by means of large-eddy simulation (LES) using a low-dissipation QR-model as formulated by Verstappen [13] and refined by Rozema [14–16]. For its use in maritime applications, see [17, 18].

The free-surface location is indicated by the Volume-of-Fluid [19] function ϕ, which evolves according to

$$\frac{\mathrm{D}}{\mathrm{D}t}\phi \equiv \frac{\partial \phi}{\partial t} + \mathbf{u}\cdot\nabla\phi = 0.$$

It is reconstructed by means of Youngs' PLIC method [20, 21].

The Navier–Stokes equations (1) are discretized on an Arakawa C-grid [22]. The second-order finite-volume discretization of the continuity equation at the 'new' time level $\cdot^{n+1}$ is given by

$$\mathsf{M}_0\mathbf{u}^{n+1} = -\mathsf{M}_\Gamma\mathbf{u}_\Gamma^{n+1}, \tag{2}$$

where M_0 acts on the interior of the domain and M_Γ acts on the boundaries of the domain (with $\mathbf{u}_\Gamma$ denoting the velocity at the boundary). In the discrete momentum equation, convection $\mathsf{C}(\mathbf{u}_h)$ and diffusion V are discretized explicitly in time. The pressure gradient is discretized at the new time level. In this exposition, for simplicity reasons the first-order forward Euler time integration will be used. In the actual calculations, a second-order Adams–Bashforth method is being applied.

Letting the diagonal matrix Ω denote the matrix containing the geometric size of the control volumes, gives the discretized momentum equation as

$$\Omega\frac{\mathbf{u}^{n+1}-\mathbf{u}^n}{\delta t} = -\mathsf{C}(\mathbf{u}^n)\,\mathbf{u}^n + \mathsf{V}\mathbf{u}^n - \mathsf{G}\mathsf{p}^{n+1} + \mathbf{f}. \tag{3}$$

For divergence-free velocity fields $\mathbf{u}$, the conservative discrete convection operator is skew-symmetric, such that convection does not contribute to energy production or dissipation; see Verstappen and Veldman [23]. In particular, its discretization preserves the energy of the flow and does not produce artificial diffusion. To make the discretization fully energy-preserving, the discrete gradient operator and the divergence operator are each other's negative transpose, i.e. $\mathsf{G} = -\mathsf{M}_0^T$, thus mimicking the analytic symmetry $\nabla = -(\nabla\cdot)^T$. In this way, also the work done by the pressure vanishes discretely.

The solution of the discrete Navier–Stokes equations is split into two steps. Firstly, an auxiliary variable $\tilde{\mathbf{u}}$ is defined through

$$\Omega \frac{\tilde{\mathbf{u}} - \mathbf{u}^n}{\delta t} = -\mathsf{C}(\mathbf{u}^n)\,\mathbf{u}^n + \mathsf{V}\mathbf{u}^n + \mathbf{f}. \tag{4}$$

With this abbreviation, the discrete momentum equation (3) can be reformulated as

$$\mathbf{u}^{n+1} = \tilde{\mathbf{u}} - \delta t\,\Omega^{-1}\mathsf{G}\mathsf{p}^{n+1}. \tag{5}$$

Secondly, by imposing discrete mass conservation (2) at the new time level, substitution of (5) results in a discrete Poisson equation for the pressure:

$$\delta t\,\mathsf{M}_0\Omega^{-1}\mathsf{G}\mathsf{p}^{n+1} = \mathsf{M}_0\tilde{\mathbf{u}} + \mathsf{M}_\Gamma\mathbf{u}_\Gamma^{n+1}. \tag{6}$$

2.2 Structural model

Based on a linear elasticity model, the deformations of an elastic structure due to stresses and body forces acting on it follow from

$$\rho_s \frac{\partial^2 d}{\partial t^2} = \nabla \cdot \overline{\overline{\sigma}}_s + f_s. \tag{7}$$

In this equation, ρ_s is the structural density, d is the vector of deformations, $\overline{\overline{\sigma}}_s$ is the second-order stress tensor and f_s is the vector body force on the structure. The stress tensor is related to the strain tensor and structural properties:

$$\overline{\overline{\sigma}}_s = C : \overline{\overline{\varepsilon}}, \tag{8}$$

where $\overline{\overline{\varepsilon}}$ is the second-order strain tensor and C is the fourth-order stiffness tensor. The strain tensor itself is related to the gradient of deformations according to

$$\varepsilon = \frac{1}{2}[\nabla d + (\nabla d)^T]. \tag{9}$$

For simplicity in this study, the structure is selected to be a one dimensional Euler–Bernoulli beam. Assuming a constant cross section A for the beam, its equation of motion is

$$\rho_s A \frac{\partial^2 d}{\partial t^2} + EI \frac{\partial^4 d}{\partial s^4} = f, \tag{10}$$

with appropriate initial and boundary conditions. Here, s denotes a coordinate along the beam, d the beam deformation, ρ_s the beam density, E Young's modulus, I the second moment of inertia and f the load per unit length of the beam.

The structural response is modeled with a finite element method. Omitting the technical details, the resulting discrete set of equations can be written in the form

$$\mathsf{M}^\mathsf{S}\ddot{\mathsf{d}} + \mathsf{K}^\mathsf{S}\mathsf{d} = \mathsf{f}, \tag{11}$$

where M^S is the discrete mass operator and K^S the discrete stiffness operator. The temporal integration of the structure equations is performed by means of the generalized-α method [24].

2.3 Fluid-solid interface

The coupling relations along the fluid-solid interface Γ_{FS} consist of two relations: the kinematic and the dynamic conditions. The kinematic condition states that the motion of the interface on both sides matches. The dynamic condition expresses equilibrium of stresses at the fluid-solid interface:

$$\text{kinematic:} \qquad u = \frac{\partial d}{\partial t} \qquad \text{on } \Gamma_{FS} \tag{12}$$

$$\text{dynamic:} \qquad \overline{\overline{\sigma}}_f \cdot n = \overline{\overline{\sigma}}_s \cdot n \qquad \text{on } \Gamma_{FS} \tag{13}$$

The dynamic condition, when the stress tensors are substituted from Eqs. (8) and (1), becomes

$$(-p\overline{\overline{I}} + \nabla \cdot (\mu \nabla u)) \cdot n = (C : \overline{\overline{\varepsilon}}) \cdot n \tag{14}$$

2.4 Time marching with subiterations

In each time step, information is exchanged between the two subsystems: the fluid solver provides the loads to the structural solver, whereas in return the latter provides the structural motion to the flow solver. In an explicit, weak coupling this exchange only happens once per time step. Below, we will dig deeper into the stability issues related to this exchange pattern. It will be explained that this proces is unstable for larger mass ratios, therefore often per time step subiterations are introduced. To make these iterations converge, severe under-relaxation may be necessary. In this way a strong coupling between the subsystems is achieved. A sketch of these subiterations (with iteration number k) per time step is given in Fig. 1.

Following [5], an Aitken-type procedure can be followed to construct a relaxation factor for which the subiterations converge. With reference to Fig. 1, in each iteration a new relaxation factor is computed from

$$\omega^{k+1} = \omega^k \, \frac{\mathsf{d}^{k-1} - \widetilde{\mathsf{d}}^k}{\mathsf{d}^{k-1} - \widetilde{\mathsf{d}}^k - (\mathsf{d}^k - \widetilde{\mathsf{d}}^{k+1})}, \tag{15}$$

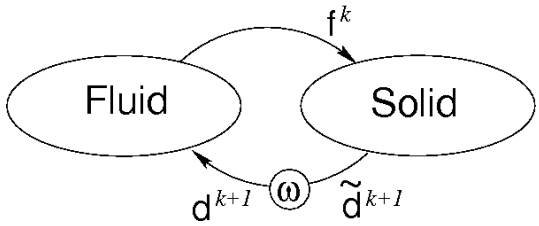

FIGURE 1. SUBITERATIVE LOOP OF FSI WITH RELAXATION WITHIN ONE TIME STEP; DISPLACEMENTS d AND k IS ITERATION LEVEL

after which the new displacement is computed as

$$\mathsf{d}^{k+1} = \mathsf{d}^k + \omega^{k+1}(\widetilde{\mathsf{d}}^{k+1} - \mathsf{d}^k). \tag{16}$$

Unfortunately, the convergence of this process can be rather slow, and each iteration a solid-fluid solve has to be performed. This makes this coupling method inefficient. In the next section we will present a method that shares the strong coupling with the above subiterations, but at a limited additional computational effort.

3 QUASI SIMULTANEOUS COUPLING

For two-way coupled problems, a monolithic procedure of the subdomains would be most powerful. However, such a simultaneous approach is not always possible, as the subdomain solvers have to be coupled at a deep iterative level. E.g. because each of the models for the subdomains can be complex, or simply because the subdomain solvers are only available as black-box. In this section we will describe an approach that tries to combine the simplicity of a hierarchical coupling approach with the iterative power of a monolithic approach.

To understand the coupling problems, the stability of the two-way coupled system is investigated in an abstract setting. On both sides of the fluid-body interface Γ_{FS} physical properties need to be continuous, as expressed in the kinematic and dynamic conditions (13) and (14). This makes it possible to formulate the coupling problem in terms of interface variables only: the velocity along the interface $\mathbf{u}_\Gamma$ and the local or total load exerted by the fluid to the structure $\mathbf{f}_\Gamma$ (for an elastic body found from the local stresses, for a solid body found from their integration along the interface).

3.1 Coupling with a solid body

Solid body - segregated coupling The solid body reacts by accelerating due to the exerted force from the fluid. For a solid body a six degrees of freedom (DOF) mass operator (M_{sb}) containing inertial properties of the body rules its dynamic response. The fluid, on the other hand, reacts to the accelerated solid body with a new pressure field. The so-called added mass operator (M_{ad}) describes the fluid's response. Thus we can formulate the coupled problem in abstract notation as

$$\text{Solid body dynamics} \qquad \mathsf{M}_{\text{sb}}\ddot{\mathbf{d}}_\Gamma^{k+1} = \mathbf{f}_\Gamma^k, \tag{17}$$

$$\text{Fluid dynamics} \qquad \mathbf{f}_\Gamma^{k+1} = -\mathsf{M}_{\text{ad}}\ddot{\mathbf{d}}_\Gamma^{k+1}. \tag{18}$$

We have already indicated the usual iterative process which is used to solve this set of, basically, 2 equations in 2 unknowns. Its formal amplification operator follows as

$$\mathbf{f}_\Gamma^{k+1} = -\mathsf{M}_{\text{ad}}\mathsf{M}_{\text{sb}}^{-1}\mathbf{f}_\Gamma^k. \tag{19}$$

The iterative procedure is stable if and only if the spectral radius of its amplification operator is less than unity, i.e. $\rho(\mathsf{M}_{\text{ad}}\mathsf{M}_{\text{sb}}^{-1}) < 1$. In other terms, the ratio of the added mass to the solid body mass for each DOF, more precisely all eigenvalues, should be less than one. If the problem violates this requirement, methods like the under-relaxation method, can only keep this value below unity at the cost of (severely) increasing computational effort.

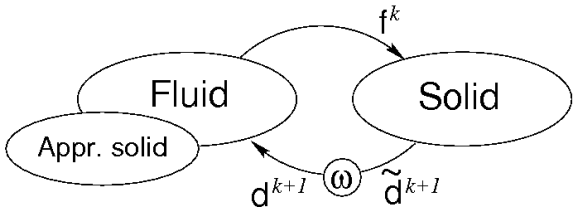

FIGURE 2. SOLID BODY AND FLUID INTERACTION WITH AN INTERACTION LAW, CONSISTING OF AN APPROXIMATE MODEL FOR THE SOLID-BODY DYNAMICS

Solid body - quasi-simultaneous coupling In the quasi-simultaneous method, exploiting the stability properties of a full monolithic approach, an approximation of the body dynamics is solved simultaneously with the fluid. This *interaction law* anticipates the body response in advance of the actual solid dynamics computation. As such, the interaction law is an approximation to the inverse mass operator ($\widetilde{\mathsf{M}_{\text{sb}}^{-1}}$) of the solid body dynamics (11). In the iterative process within each time step, the interaction law is exploited as

$$\text{Solid-body} \qquad \ddot{\mathbf{d}}_\Gamma^{k+1} = \mathsf{M}_{\text{sb}}^{-1}\mathbf{f}_\Gamma^k, \tag{20}$$

$$\text{Interaction law} \qquad \dot{\mathbf{u}}_\Gamma - \widetilde{\mathsf{M}_{\text{sb}}^{-1}}\mathbf{f}_\Gamma^{k+1} = \ddot{\mathbf{d}}_\Gamma^{k+1} - \widetilde{\mathsf{M}_{\text{sb}}^{-1}}\mathbf{f}_\Gamma^k, \tag{21}$$

$$\text{Fluid} \qquad \mathbf{f}_\Gamma^{k+1} + \mathsf{M}_{\text{ad}}\dot{\mathbf{u}}_\Gamma = 0. \tag{22}$$

Eliminating the appearances of $\mathbf{u}_\Gamma$ leads to the following iterative process, which can be compared to (19):

$$\left\{ \mathsf{I} + \mathsf{M}_{\mathrm{ad}} \widetilde{\mathsf{M}_{\mathrm{sb}}^{-1}} \right\} \mathbf{f}_\Gamma^{k+1} = -\mathsf{M}_{\mathrm{ad}} \left\{ \mathsf{M}_{\mathrm{sb}}^{-1} - \widetilde{\mathsf{M}_{\mathrm{sb}}^{-1}} \right\} \mathbf{f}_\Gamma^{k}, \qquad (23)$$

where I is the unit operator. In heuristic terms, the addition of the interaction law makes the left-hand side larger and the right-hand side smaller, thus improving the convergence. In more mathematical terms, the interaction law should neutralize the most cumbersome eigenvalues of the iteration matrix.

3.2 Elastic body coupling

Next, the same procedure is repeated for an elastic body whose deformation is governed by Eq. (11). Because this equation contains both $\ddot{\mathsf{d}}$ and d, first a discrete time integration is carried out. Thereafter, with similar notation as before, but now the operators are locally defined along the interface, the discrete version of the hierarchically coupled problem at the new time level can be denoted as

$$\text{Elastic body} \qquad \left(\frac{\mathsf{M}_{\mathrm{eb}}}{\delta t^2} + \mathsf{K}_{\mathrm{eb}} \right) \mathbf{d}_\Gamma^{k+1} = \mathbf{f}_\Gamma^{k}, \qquad (24)$$

$$\text{Fluid} \qquad \mathbf{f}_\Gamma^{k+1} = -\frac{\mathsf{M}_{\mathrm{ad}}}{\delta t^2} \mathbf{d}_\Gamma^{k+1}. \qquad (25)$$

Here, M_{eb} generalizes the discrete elastic body mass operator, while K_{eb} is the discrete elastic body stiffness operator. The contributon from the previous time steps is omitted in view of clarity; it is just an inhomogeneous term in the right-hand side, which is not relevant for the convergence of the subiterations per time step.

Matrices M_{eb} and K_{eb} can be simultaneously diagonalized as $\mathsf{Q}^T \mathsf{M}_{\mathrm{eb}} \mathsf{Q} = \mathsf{I}$ and $\mathsf{Q}^T \mathsf{K}_{\mathrm{eb}} \mathsf{Q} = \Lambda$. Here, Q contains the normalized elastic body eigenvectors with eigenvalues Λ. In this way, the elastic body dynamics (24) can be rewritten as

$$\text{Elastic body} \qquad \mathsf{Q}^{-T} \left(\frac{\mathsf{I}}{\delta t^2} + \Lambda \right) \mathsf{Q}^{-1} \mathbf{d}_\Gamma^{k+1} = \mathbf{f}_\Gamma^{k}. \qquad (26)$$

In this formulation, we recognize the modal participation factors $\mathsf{z}_\Gamma \equiv \mathsf{Q}^{-1} \mathbf{d}_\Gamma$.

The displacement $\mathbf{d}^{k+1}$ can be eliminated from the system of equations (25 and (26), after which the iterative process can be written as

$$\mathbf{f}^{k+1} = -\mathsf{M}_{\mathrm{ad}} \mathsf{Q} (\mathsf{I} + \delta t^2 \Lambda)^{-1} \mathsf{Q}^T \mathbf{f}^{k}. \qquad (27)$$

For small enough δt, the amplification factor simplifies to $\mathsf{M}_{\mathrm{ad}} \mathsf{Q}\mathsf{Q}^T$, where $\mathsf{Q}\mathsf{Q}^T$ has the dimension of $1/kg$. For a solid body with 6 DOF this relation resembles Eq. (19), and therefore $\mathsf{Q}\mathsf{Q}^T$ has a similar role as $\mathsf{M}_{\mathrm{sb}}^{-1}$.

Elastic body - quasi-simultaneous coupling The analogy with solid-body motion suggests to derive an interaction law built from the lowest elastic modes of the structure, i.e. we define an approximation $\widetilde{\mathsf{Q}}$ by only retaining the first few eigenvectors. These correspond with the largest eigenvalues in Λ, i.e. the lowest natural frequencies, which will be collected in $\widetilde{\Lambda}$. These modes are usually also the ones with the highest modal added mass.

Proceeding in this way, the proposed interaction law reads

$$\mathbf{d}^{k+1} - \widetilde{\mathsf{Q}} \left(\frac{1}{\delta t^2} + \widetilde{\Lambda} \right)^{-1} \widetilde{\mathsf{Q}}^T \mathbf{f}^{k+1} = \left\{ \mathsf{Q} \left(\frac{1}{\delta t^2} + \Lambda \right)^{-1} \mathsf{Q}^T - \widetilde{\mathsf{Q}} \left(\frac{1}{\delta t^2} + \widetilde{\Lambda} \right)^{-1} \widetilde{\mathsf{Q}}^T \right\} \mathbf{f}^{k}.$$

Letting $\delta t \to 0$, i.e. studying zero-stability, and combining with the fluid-flow model (25), the quasi-simultaneous iterative process reduces to

$$\mathbf{f}^{k+1} = -(\mathsf{M}_{\mathrm{ad}}^{-1} + \widetilde{\mathsf{Q}}\widetilde{\mathsf{Q}}^T)^{-1} (\mathsf{Q}\mathsf{Q}^T - \widetilde{\mathsf{Q}}\widetilde{\mathsf{Q}}^T) \mathbf{f}^{k}. \qquad (28)$$

Clearly, if all of the modes are incorporated into the interaction law, the spectral radius will become zero and the method simultaneously solves the fluid with the 'exact' body.

3.3 Implementation

The interaction law is a relation between the pressure and the local velocity of the body surface. This relation can be substituted in the right-hand side of the discrete mass equation (2). Thus it becomes a boundary condition for the discrete Poisson equation. It can be shown that the latter retains it favourable numerical properties (symmetric, negative definite), such that its iterative solution can proceed as before.

4 EXAMPLES

4.1 Falling life boat

The first test case is a simulation of a 6-DOF life boat dropped into a large wave - Fig. 3. The fluid flow is solved on a grid consisting of about 0.7 million active (= fluid) grid points, with local grid refinement [25, 26] around the life boat. For physical accuracy this grid is rather coarse, as the focus in these simulations is on the numerical behaviour of the coupling process. Both the weak coupling procedure (19) as well as the quasi-simultaneous procedure (23) have been applied.

Relevant is the amount of work needed per time step to achieve the coupling between solid-body dynamics and fluid

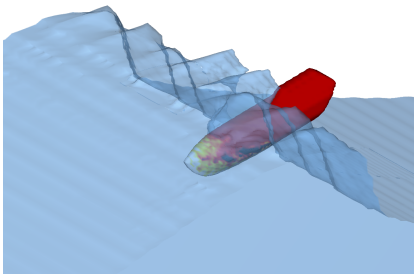

FIGURE 3. SNAPSHOT OF A LIFE BOAT FALLING INTO A LARGE WAVE

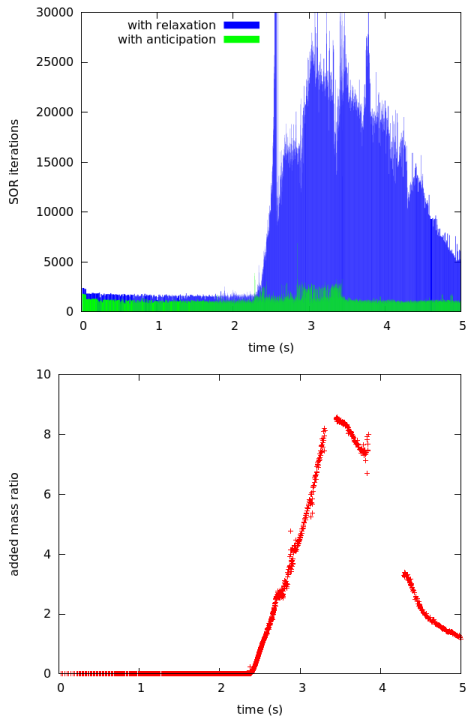

FIGURE 4. *TOP:* THE NUMBER OF SOR ITERATIONS PER TIME STEP FOR THE UNDERRELAXED WEAK COUPLING METHOD (BLUE) AND THE ANTICIPATORY QUASI-SIMULTANEOUS METHOD (GREEN)). *BOTTOM:* THE ESTIMATED ADDED MASS FOR THE FALLING LIFEBOAT AS A FUNCTION OF TIME. THE CROSSING OF THE FREE SURFACE IS CLEARLY VISIBLE IN THE ADDED MASS

flow. The weak method often requires dozens of subiterations, in each of which a Poisson equation has to be solved. This number is dependent on the amount of fluid that is moved aside by the moving body, represented by the added-mass operator M_{ad}. The later subiterations have a good initial guess so they are not as expensive as the earlier ones. Thus the amount of work is better represented by the total number of (in this example SOR [27]) iterations needed for all Poisson solves within one time step.

This amount of work is shown in Fig. 4(top). The relation with the added mass becomes visible when plotting the time history of the estimated added mass in Fig. 4(bottom). [The 'gaps' in the curve are due to a loss of significant digits during the post-processing to estimate the added mass.] Comparison with Fig. 4(top) shows clearly that the number of iterations grows rapidly when the 'added-mass ratio' $\mathsf{M}_{\mathrm{ad}}\mathsf{M}_{\mathrm{sb}}^{-1}$ growths beyond 1. In contrast, the quasi-simultaneous method requires one or two subiterations, resulting in much less work per time step (Fig. 4(bottom)). The number of subiterations is independent of the grid size and of the Poisson solver, as it is determined by the difference between the analytic pendants of M_{sb} and $\widetilde{\mathsf{M}_{\mathrm{sb}}^{-1}}$.

Although the added mass varies greatly over time during the impact, and the relaxation method (19) is highly sensitive, the anticipative method (23), remains efficient. In this example, the workload is reduced by a factor around 10 for the complete simulation.

4.2 Solid body: CALM buoy

The second case is a validation against model tests of a CALM buoy (Fig. 5) in a shallow water basin at MARIN [28]. These tests include the freely decaying motion of the buoy after being released from a given position into calm water. This allows us to compare the simulated and measured natural periods as well as the amount of hydrodynamic damping.

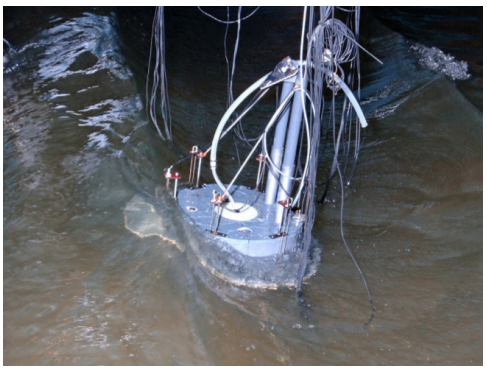

FIGURE 5. MODEL OF THE CALM BUOY IN THE SHALLOW WATER BASIN AT MARIN

The buoy in its default configuration has been modelled as a cylinder with a diameter of 12 m and a height of 6.5 m. The simulation has been performed at different grids, with approximately 6, 10 and 18 cells per cylinder diameter. For the heave motions, the natural period is well-predicted by the simulation at a grid resolution of 18 cells per diameter (see Fig. 6). The damping however is incorrect and needs finer resolution.

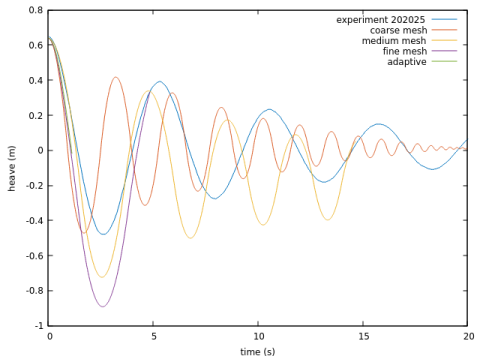

FIGURE 6. HEAVE MOTIONS OF A FREE-FLOATING CALM BUOY IN SIMULATION AND EXPERIMENT

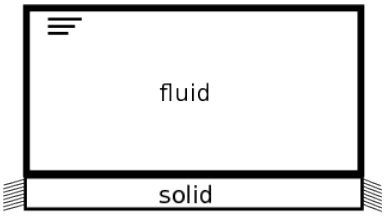

FIGURE 7. SCHEMATIC OF THE FIRST TEST CASE; THE DOMAIN WITH FREE-SURFACE FLOW ON TOP AND FLEXIBLE BEAM AT THE BOTTOM

4.3 Elastic body: tank with membrane bottom

In order to assess the performance of the quasi-simultaneous approach for different mass ratios, a test case has been designed in which this ratio can be varied.

At the bottom of a rectangular container ($1.0 \times 0.1 \times 0.5\,\mathrm{m}^3$) filled with 50 kg of water, a flexible beam is placed as illustrated in Fig.7. The mass of the beam is varied between 1 kg and 50 kg; its module of elasticity is 1 MPa. The interaction law is made out of truncated structural modes; the number of modes dictates its accuracy. The relaxation parameter is adjusted by Aitken's method. Five cases with different mass ratios are solved with and without the interaction law. Also, the effect of the accuracy of the interaction law on the performance is studied.

Effect of mass ratio First, the effect of the added mass ratio is studied. The interaction law is constructed out of the first 10 modes, while the symmetry of the problem cancels out the effect of odd modes. For all the cases the initial relaxation parameter is set to 1, while from the third FSI iteration this value is adjusted by Aitken's method. Fig. 8 shows the convergence of the FSI iterations during the first time step. As shown in Fig. 8(a), higher mass ratios require more computational effort. Plugging in the interaction law, Fig. 8(b) reproduces the same solution while the computational effort is less. It can be observed that the difficult cases with higher mass ratios speed-up a lot more from the quasi-simultaneous approach than the easier cases with modest mass ratios. The tuned Aitken relaxation parameters as well as the

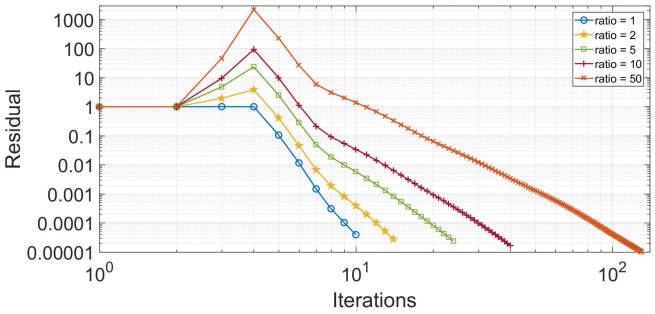

(a) Convergence history without the interaction law

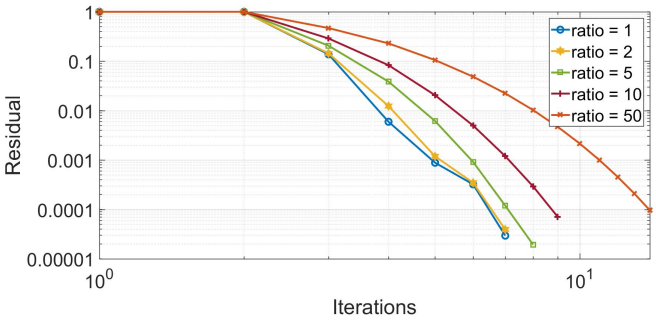

(b) Convergence history with the interaction law

FIGURE 8. CONVERGENCE HISTORY FOR THE FIRST TIME STEP FOR DIFFERENT ADDED MASS RATIOS

convergence rates are summarized in Table 1 for both methods. The difference in convergence rates is clearly visible, with the quasi-simultaneous method hardly needing any underrelaxation.

	conventional method		quasi-simultaneous method	
mass ratio	relaxation	conv. rate	relaxation	conv. rate
1	0.45	0.36	0.94	0.05
2	0.30	0.51	0.95	0.09
5	0.15	0.72	0.96	0.08
10	0.08	0.83	0.96	0.24
50	0.01	0.96	0.97	0.46

TABLE 1. AITKEN RELAXATION PARAMETER AND CONVERGENCE RATE FOR CONVENTIONAL AND QUASI-SIMULTANEOUS METHOD

Effect of number of modes The effect of the number of modes in the interaction law is shown in Fig.9. Obviously, employing more modes improves the structure response estimation in the interaction law. But there is a trade off, as the gain goes down while making the interaction law itself more expensive. When the mass ratio is low, the number of effective modes is lower than the case when mass ratio is 50.

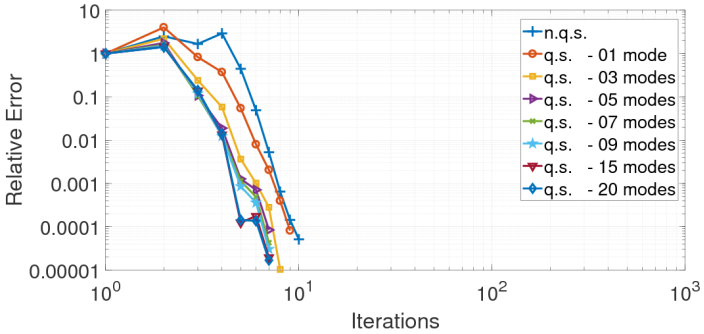

(a) Convergence history for added mass ratio 1

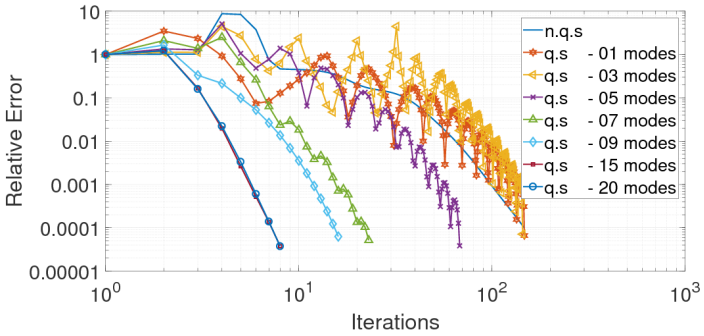

(b) Convergence history for added mass ratio 50

FIGURE 9. CONVERGENCE HISTORY FOR THE FIRST TIME STEP FOR DIFFERENT ACCURACY OF INTERACTION LAWS

4.4 Rubber gate

The validation test case is an elastic rubber gate placed in front of a bulk of water. This experiment has been performed by Antoci [29]. The simulation is done with and without the interaction law and the results are compared.

Setup The gate separating the fluid from the air is partly rigid, but the lower part is elastic as shown in Fig. 10. The rubber gate is clamped on the top side and free on the other side. The density of the beam is $\rho_s = 1100$ kg/m^3 and the Young modulus for elasticity is $E = 10$ MPa. The dimensional properties of the domain is presented in Table 2. According to [29], the problem is

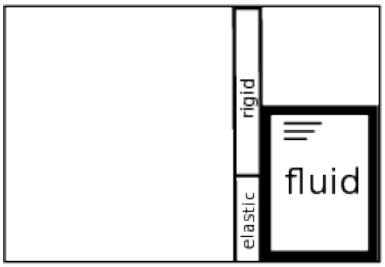

FIGURE 10. SCHEMATIC VIEW OF THE RUBBER GATE TEST CASE

geometrical parameter	length (m)
initial water height	0.14
elastic gate length	0.079
tank length	0.01
gate thickness	0.005
tank width	0.01

TABLE 2. GEOMETRICAL PROPERTIES OF THE RUBBER GATE TEST CASE

mostly two dimensional, so in the current study numerical simulations are performed in 2D. A grid of $250 \times 2 \times 50$ is used. The initial time step is set to be 1×10^{-4}; this value is automatically adjusted during the simulation based on the Courant condition.

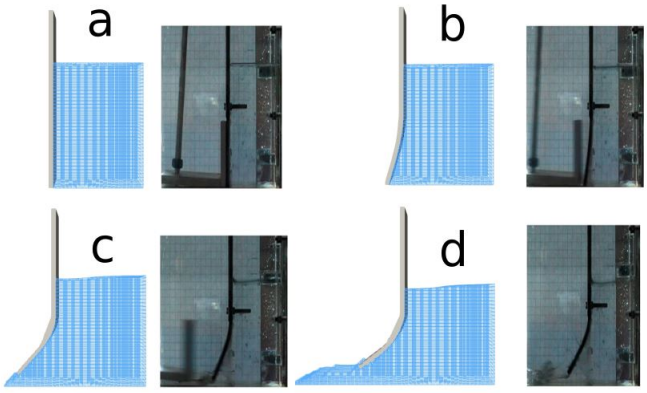

FIGURE 11. SNAPSHOTS OF THE SIMULATION PAST A RUBBER GATE, COMPARED WITH THE EXPERIMENT OF [29]

Results The results after 0.12 s are presented, the snapshots from experiment and simulation at time intervals of 0.4 s are compared in Fig. 11. As shown in Fig. 12, the vertical and

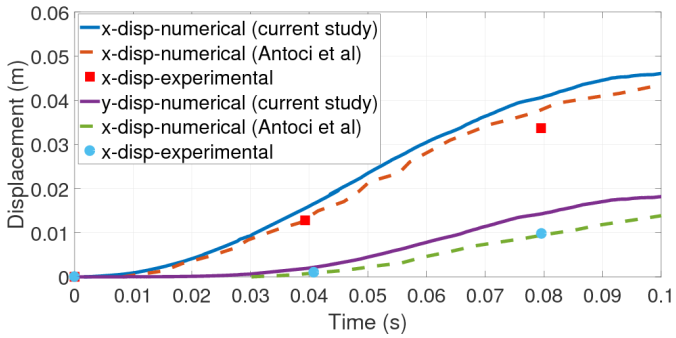

FIGURE 12. DISPLACEMENT OF THE TIP OF THE RUBBER GATE: SIMULATION VERSUS EXPERIMENT

horizontal displacement of the free side of the rubber gate is calculated and it is in good agreement with the experimental data. The difference is mainly due to the uncertainty in modulus of elasticity for the rubber which was measured ([29] also varied the elasticity to achieve the best agreement with experimental results). In this research, the original value of 10 MPa is adopted.

The water height behind the gate is measured during experiment and compared with numerical results of this study in Fig. 12. The linear model for the elastic gate is mainly responsible for mismatch between the measured water height and the calculated values.

5 CONCLUSION

It has been demonstrated that the ratio of the fluid added mass versus the solid-body mass is an important parameter, controlling the (in)stability of a fluid-structure system. Whereas traditional (sub)iteration methods require severe underrelaxation, a quasi-simultaneous method can handle large added mass ratios more efficiently. An interaction law approximating the structural dynamics is its key ingredient. It is shown that only a couple of dominant modes are needed to achieve a stable method. The stability and resulting efficiency is demonstrated by comparing the computational effort with and without interaction law on a number of offshore-related applications.

6 ACKNOWLEDGMENTS

This work is part of the research programme Maritime2013 with project number 13267 which is (partly) financed by the Netherlands Organisation for Scientific Research (NWO).

REFERENCES

[1] Veldman, A. E. P., 2009. "A simple interaction law for viscous-inviscid interaction". *J. Eng. Math.,* ***65***, pp. 367–383.

[2] Fekken, G., Veldman, A. E. P., and Buchner, B., 1999. "Simulation of green-water loading using the Navier-Stokes equations". In Proc. 7th Int. Conf. Numer. Ship Hydrodyn., J. Piquet, ed., pp. 6.3–1–6.3–12.

[3] Causin, P., Gerbau, J. F., and Nobile, F., 2004. Added-mass effect in the design of partitioned algorithms for fluid-structure problems. ICES Report 04-02. Le Chesnay (France).

[4] Benra, F., Dohmen, H. J., Pei, J., Schuster, S., and Wan, B., 2011. "A comparison of one-way and two-way coupling methods for numerical analysis of fluid-structure interactions". *J. Appl. Math.,* ***2011***, pp. 1–16.

[5] Forster, C., Wall, W. A., and Ramm, E., 2006. "Artificial added mass instabilities in sequential staggered coupling of nonlinear structures and incompressible viscous flows". *J. Comp. Meth. Appl. Mech. Eng.,* ***196***, pp. 1278–1293.

[6] Veldman, A. E. P., 2001. "Matched asymptotic expansions and the numerical treatment of viscous-inviscid interaction". *J. Eng. Math.,* ***39***, pp. 189–206.

[7] Fletcher, C. A. J., 1988. *Computational Techniques for Fluid Dynamics*, Vol. 2: *Specific Techniques for Different Flow Categories*. Springer-Verlag, Berlin.

[8] Kleefsman, K. M. T., Fekken, G., Veldman, A. E. P., Iwanowski, B., and Buchner, B., 2005. "A Volume-of-Fluid based simulation method for wave impact problems". *J. Comput. Phys.,* ***206***, pp. 363–393.

[9] Veldman, A. E. P., Gerrits, J., Luppes, R., Helder, J. A., and Vreeburg, J. P. B., 2007. "The numerical simulation of liquid sloshing on board spacecraft". *J. Comput. Phys.,* ***224***, pp. 82–99.

[10] Veldman, A. E. P., Luppes, R., Bunnik, T., Huijsmans, R. H. M., Duz, B., Iwanowski, B., Wemmenhove, R., Borsboom, M. J. A., Wellens, P. R., van der Heiden, H. J. L., and van der Plas, P., 2011. "Extreme wave impact on offshore platforms and coastal constructions". In Proc. 30th Conf. Ocean, Offshore Arctic Eng. OMAE2011. Paper OMAE2011-49488.

[11] Veldman, A. E. P., Luppes, R., van der Heiden, H. J. L., van der Plas, P., Duz, B., and Huijsmans, R. H. M., 2014. "Turbulence modeling, local grid refinement and absorbing boundary conditions for free-surface flow simulations in offshore applications". In Proc. 33rd Int. Conf. Ocean, Offshore and Arctic Eng. Paper OMAE2014-24427.

[12] Wemmenhove, R., Luppes, R., Veldman, A. E. P., and Bunnik, T., 2015. "Numerical simulation of hydrodynamic wave loading by a compressible two-phase flow method". *Computers & Fluids,* ***114***, pp. 218–231.

[13] Verstappen, R., 2011. "When does eddy viscosity damp

subfilter scales sufficiently?". *J. Sci. Comput.,* ***49***(1), pp. 94–110.

[14] Rozema, W., 2015. "Low-dissipation methods and models for the simulation of turbulent subsonic flow". PhD thesis, University of Groningen.

[15] Rozema, W., Bae, H. J., Moin, P., and Verstappen, R., 2015. "Minimum-dissipation models for large-eddy simulation". *Phys. Fluids,* ***27***, p. 085107.

[16] Abkar, M., Bae, H. J., and Moin, P., 2016. "Minimum-dissipation scalar transport model for large-eddy simulation of turbulent flows". *Physical Review Fluids,* ***1***(4), p. 041701.

[17] van der Heiden, H. J. L., Veldman, A. E. P., Luppes, R., van der Plas, P., Helder, J., and Bunnik, T., 2015. "Turbulence modeling for free-surface flow simulations in offshore applications". In Proc. 34th Int. Conf. Ocean, Offshore and Arctic Eng. OMAE2015. Paper OMAE2015-41078.

[18] Veldman, A. E. P., Luppes, R., van der Plas, P., van der Heiden, H. J. L., Helder, J., and Bunnik, T., 2015. "Turbulence modeling for locally-refined free-surface flow simulations in offshore applications". In Proc. 25th Int. Symp. Offshore and Polar Eng. ISOPE2015. Paper ISOPE2015-TPC-0282.

[19] Hirt, C. W., and Nichols, B. D., 1981. "Volume of fluid (VOF) method for the dynamics of free boundaries". *J. Comput. Phys.,* ***39***, pp. 201–25.

[20] Youngs, D. L., 1987. An interface tracking method for a 3d Eulerian hydrodynamics code. Technical Report AWRE/44/92/35, Atomic Weapons Research Establishment.

[21] Düz, B., 2015. "Wave generation, propagation and absorption in CFD simulations of free surface flows". PhD thesis, Technical University Delft.

[22] Arakawa, A., 1966. "Computational design for long-term numerical integration of the equations of fluid motion: Two-dimensional incompressible flow. part I". *J. Comput. Phys.,* ***1***, pp. 119–143.

[23] Verstappen, R. W. C. P., and Veldman, A. E. P., 2003. "Symmetry-preserving discretization of turbulent flow". *J. Comput. Phys.,* ***187***, pp. 343–368.

[24] Chung, J., and Hulbert, G. M., 1992. "A time integration algorithm for structural dynamics with improved numerical dissipation: the generalized-α method". *J. Appl. Mech.,* ***60***(2), pp. 371–375.

[25] van der Plas, P., Veldman, A. E. P., van der Heiden, H. J. L., and Luppes, R., 2015. "Adaptive grid refinement for free-surface flow simulations in offshore applications". In Proc. 34th Int. Conf. Ocean, Offshore and Arctic Eng. OMAE2015. Paper OMAE2015-42029.

[26] Veldman, A. E. P., van der Plas, P., Seubers, H., Helder, J., and Lam, K.-W., 2018. "Adaptive grid refinement for two-phase offshore applications". In Proc. 37th Int. Conf. Ocean, Offshore and Arctic Eng. OMAE2018. Paper OMAE2018-77309.

[27] Botta, E. F. F., and Ellenbroek, M. H. M., 1985. "A modified SOR method for the Poisson equation in unsteady free-surface flow calculations". *J. Comput. Phys. ,* ***60***, pp. 119–134.

[28] Bunnik, T. H. J., and van Doeveren, A. G., 2008. CALM buoy model tests. Tech. Rep. report 18378-3-BT, MARIN.

[29] Antoci, C., Gallati, M., and Sibilla, S., 2007. "Numerical simulation of fluidstructure interaction by SPH". *J. Comp. Struct.,* ***85***, pp. 879–890.